Research Report on “Facial Recognition through Eye Spacing Measurement”

Mark Nixon

Dept. of Electronics and Information Engineering, University of Southampton, Highfield, Southampton, England, SO9 5NH

***Abstract*—Facial recognition has been an inveterate problem in the field of image processing and computer vision. Automated facial recognition has been implemented much in field of image processing research by measuring geometric features of human face and eye spacing measurement has been recognized as a suitable step in fulfilling this objective. Hough Transform has been used a lot in detecting the edges of objects of different shapes. Eye spacing measurement has been done as an application of Hough transform to detect the presence of a circular shape and an ellipsoidal shape which corresponds to the perimeter of the iris, sclera and the region below the eyebrows. Presence of noise in the feature space were removed using the magnitude and direction of gradient. Experimental results prove that spacing measurement through detection of iris is the most accurate method and through the detection of the position of eyebrows is the least accurate method even though it is associated with less constraints. Usage of these techniques led to the measurement of characteristic features of human face with sufficient accuracy.**

Keywords—face detection, hough transform, image processing, eye spacing measurement, computer vision

I. INTRODUCTION

Image processing is one of the key terms which is driving automation, security and safety related application of the electronic industry. In the task of managing with the most demanding quality control challenges, the human eye alone can no longer survive alone. Gigantic image processing solutions has become ever more complicated nowadays, but have served as an immense help for solving many problems in real time applications. Facial recognition has been one of such problems which fascinated researchers for several years. Much study has been made in this field and several automated methods has been proposed to achieve this goal. An early attempt in this field was a device which used the network of photomultipliers to learn the pattern of each face. Automatic recognition using facial profile were the later attempts in this field, which has two methods, one concerned with the description of facial profile using 17 fiducials and the other method was recognition via a profile silhouette whose twelve components were obtained using a circular autocorrelation function. One of the later attempts used artificial neural networks and machine learning to distinguish between different subjects. Measurement of geometric features of human face has been identified as a crucial factor for the facial recognition problem. A panel of observers classified faces according to a set of criteria using three portraits of each face comprising a frontal, side and a three-quarter profile. Following the classification, several criteria were rejected as being unsuitable for recognition. The measures for each face of the remaining criteria were then sorted by computer which usually required six arrangements to isolate a single face. Most basic features such as length and protrusion of ears, lip thickness, eye separation and shade, nose profile and mouth width were used for analysis and out of all these, the eye spacing measurement was the most intriguing feature since it offers a distinct feature within the face. In this paper, the spacing between the eyes is measured using Hough transform to detect the shape of distinct parts of the eye.

II. APPLICATION OF THE HOUGH TRANSFORM

A. The Hough Transform

Hough Transform technique is the most suitable method for feature extraction among all the feature extraction techniques available, mainly because of its noise tolerant ability. Analytically described shapes were recognized using the magnitude of gradient information alone in the early days and later, directional information obtained from the gradient is also used for the detection process. Feature extraction is to be initially applied to an image to generate the feature space in which the required shape is to be detected. An array of accumulators is defined in which each element is indexed by a particular set of values for each parameter. The limitations on each parameter decides the dimension of this array and each point in the array is incremented for each point in the feature space which is present on the required shape described by that set of parameters and is sufficient in terms of gradient strength and direction.

Consider a point (x,y) on the shape to be detected, described by the set of parameters p1,p2,p3 etc,

Then, feature(p1,p2,…) = feature(p1,p2,…) + 1

If the gradient magnitude,
$\sqrt{(df(x,y)/dx)2 + (df(x,y)/dy)2} \geq$ threshold

and the direction, $\tan^{-1}[(df(x,y)/dy/df(x,y)/dx)] = \phi$

where ϕ is determined by the position of the point (x,y) in the analytically defined shape.

B. Definition of shapes appropriate for detection

Two features of the eye are used for analysis such as the perimeter of the iris and the perimeter of the sclera or the white part. The iris is round and therefore detection of circular shape is a task which is already done in Image Processing. The limitation is that if the eyes are closed or if the iris are in extreme positions, detection is difficult. Measuring the perimeter of the sclera has the advantage that the shape of this feature is reflected in the shape of the region below the eyebrows which allows eye spacing measurements even in the case of closed eyes. Therefore, recognition is done by considering both the factors mentioned above.

Shape representing the iris is a circle and is shown in Figure 1. The perimeter of the sclera would approximate an ellipse, but is unsatisfactory for those parts of the eye which are farthest from the center of the face. Shape of the ellipse is tailored using an exponential function for this reason. This tailored exponential function is shown in Figure 2.

Analytic definition of both shapes is thus:

Iris (both eyes)

$$Y=Y_0\pm\sqrt{r2-(x-x0)2} \qquad X_0-r \leq X \leq X_0+r \qquad (1)$$

Where X_0 and Y_0 are the co-ordinates of the center and r represents the radius.

Perimeter of sclera (right eye)

$$y = y_0 \pm y_r \sqrt{1 - (x - x_0)^2/x_r^2} \qquad x_0-r \leq x \leq x_0 \qquad (2)$$

$$y = y_0 \pm y_r \exp(-(x - x_0)^2/r^2) \qquad x_0 < x \leq x_0 + r \qquad (3)$$

Where Xr and Yr are the major and the minor axes respectively. For the shape approximating the perimeter of the sclera of the left eye the restrictions on x in eqn. 2 and eqn. 3 are interchanged.

The general rotational transformation may be used namely

$$\begin{bmatrix} x' \\ y' \end{bmatrix} = \begin{bmatrix} \cos\theta & \sin\theta \\ -\sin\theta & \cos\theta \end{bmatrix} \begin{bmatrix} x \\ y \end{bmatrix} \qquad (4)$$

Where X' and Y' are the co-ordinates of the rotated ellipse and ϕ the angle of rotation.

It is difficult to determine whether each point in the image lies on a circle defined by a particular set of parameters. For quick computation, it is advised to calculate the coordinates of each point which may lie on a shape indexed by a particular set of parameters. This is easier because, the shape of the circle is reflected around both central axes implying that the points for one quadrant only need be calculated, the points in the other quadrants being reflections around the major axes of the circle. For this reason, computation for the value of the x coordinates for increments in the y coordinate, for each shape given yn = yo ± n (n € l,2,...y r), calculation is based on

$$\text{circle} \qquad x_n = x_0 \pm \sqrt{r^2 - n^2} \qquad (5)$$

$$\text{ellipse} \qquad x_n = x_0 \pm x_r \sqrt{1 - (n/y_r)^2} \qquad (6)$$

$$\text{tailored part of ellipse} \qquad x_n = x_0 \pm x_r \sqrt{-\log(ky_r + n)/y_r} \qquad (7)$$

Where k=0.368. A derivation of equation 5 is presented in the appendix. Calculation also takes advantage of the reflection of each shape. A similar set of equations may be generated for calculation of each y coordinate given increments in the x coordinate. Figure 6 illustrates the match of the tailored ellipse to the perimeter of the sclera. This shape can be modified further to compensate for the slight mismatch of the extremity of the eye. The shape of the tailored ellipse is satisfactory also for detection of the position of the region below the eyebrows. Fortunately, gradient directions at the perimeter of the eyebrow are the same as those for the perimeter of the sclera because the eyebrow is darker than the interior part of the eye. However, the center of this shape when used to approximate the eyebrows naturally differs from the center of the shape of the sclera.

III. Implementation

These techniques have been implemented using a DEC PDF LSI 11/23 microcomputer based image processing development system which runs the SAIDIE suite of image processing software under the RT 11 operating system. This system offers facility to process images of 128 x 128 pixels of 256 grey levels.

IV. Application

Initially, the gradient image is to be generated for locating the desired features. Figure 4 was obtained using the Sobel gradient operator on Figure 3. Thresholding was done at a strength of 4 brightness values on the gradient magnitude. Figure 4 depicts the direction of the gradient. The process of detection of eyes location has a limitation that half of the image in which the eye must be present. Other limitations on the magnitude were created using a wide data set. A generalized control strategy is the expected to develop in future for the purpose of facial recognition.

V. RESULTS

The Hough Transform was applied to an image to identify the presence of each shape in a limited data of six subjects. Results were obtained in the same illumination conditions and two images with full frontal views in such a way that center of each face approximately coincided with the center of the image, were taken for consideration. Position of iris is shown in Figure 5 and the results in Table 1 shows that there is not much difference between the detected position of the center of each iris and their estimated values. The measured eye spacing was close to the estimated spacing, with the difference being 0.33 pixels, which shows a good accuracy. The perimeter of the shape of the region below the eyebrows is sown in Figure 7. Table 2 shows the spacing measurements provided by the detection of eyebrows and these results reveal a wider spacing. This spacing is approximately 20% over that measurement provided by the detection of irises. The central co-ordinates of the perimeter of the sclera is shown in Figure 6 and the spacing measurements are given in Table 2. The difference between the measured spacing and estimated spacing was an average difference of -1.33 pixels. It should be noted that the results for detection of the perimeter of the sclera for subject 3 and subject 5 were not derived by global application of the Hough transform. Unfortunately, the shape of the perimeter of the sclera may sometimes occur in the region of the eyebrows if the eyebrows lift towards the exterior of the face. Results prove that, measurement of eye spacing by the detection of the irises and the shape illustrating the perimeter of the sclera and the eye brows is possible through the application of Hough Transform. Most accurate method among all the techniques used is the measurement of spacing by the detection of position of irises, next is the method of detecting the perimeter of the sclera, which is a sensitive method and the least accurate is the technique of the detection of the position of eyebrows.

VI. FURTHER WORK

Automated facial recognition can be established by the development of a generalized control strategy in a full package. Application of these techniques can be used to employ the detection of the position of eyebrows with constraints derived by the location of the perimeter of the face. This information can be further modified for the recognition of iris and sclera. Optimization of the Hough Transform has the possibility to reduce the burden of computational complexity and makes the algorithm faster.

VII. CONCLUSION

Hough Transform was used for the measurement of various eye spacing and for detecting the shapes of various distinct parts of the eye. The spacing between the centers of both the iris in the human face has been done by measuring the perimeter of the circular shaped iris with suitable brightness profile. These measurements were approximately close to the calculated/estimated values. The perimeter of both the sclera and the shape of the region below the eyebrows were also measured. The calculation based on approximation to the eyebrows shape was least constrained, but was consistently in excess of those provided by other methods. The issue of noise contaminating the feature space was solved by using Hough Transform technique which includes gradient strength and gradient direction. This method was formulated in a computationally efficient manner. These methods have a lot of applications which led to the measurement of eye spacing. This measurement can be used to distinguish between different subjects with a good amount of accuracy. Automated facial recognition is possible in future with a full package of all these techniques in an organized manner.

VIII. APPENDIX

A. Development of Equation 5

To calculate the complete set of points which lie on a circle center (Xo,Yo) with radius r either polar or cartesian rotation may be used. For cartesian coordinates,

Given, $Y=Y_0\pm\sqrt{r2 - (x - x0)2}$

for Y1 = Y0, X1 = X0 - r (point on y axis on left side of circle), for Yn = Yo + n where n is an integer (n = 1, 2, 3..)

$n = \sqrt{r2 - (Xn - X0)2}$

where, Xn = X0 – r + ΔXn

with solution, $\Delta Xn = r \pm \sqrt{r2 - n2}$

A similar method may be used to generate eqns. 6 and 7

Table 1 Coordinates of Centre of Iris

Subject	Estimated Coordinates (±1 pixel)		Measured Coordinates	
	Left Eye	Right Eye	Left Eye	Right Eye
1	31,37	96,38	31,38	96,39
2	36,44	100,43	36,44	101,43
3	40,41	97,43	40,42	97,44
4	25,35	90,35	24,34	89,36
5	30,48	91,50	30,50	92,49
6	29,41	95,45	29,41	95,45

All measurements in pixels

Table 2 Eye Spacing Measurements

Subject	Estimated Spacing (±2 pixels)	Spacing by Irises	Spacing by Perimeter of Sclera	Spacing by Eyebrows	Eyebrow Spacing/ Estimated Spacing
1	65	65	63	80	1.23
2	64	65	63	79	1.23
3	57	57	60	72	1.26
4	65	65	60	76	1.17
5	61	62	60	76	1.25
6	66	66	64	74	1.12

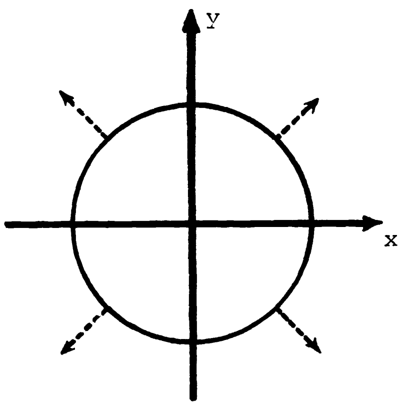

Fig. 1 Circle showing gradient directions for iris (dotted)

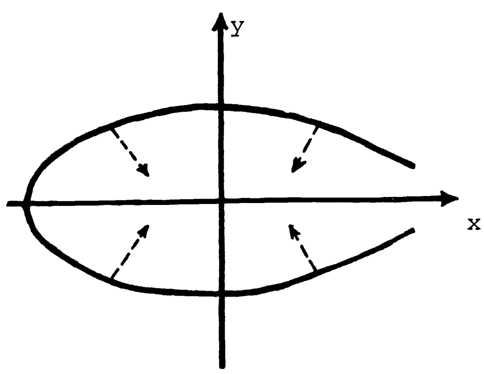

Fig. 2 Shape approximating perimeter of sclera showing gradient directions (dotted)

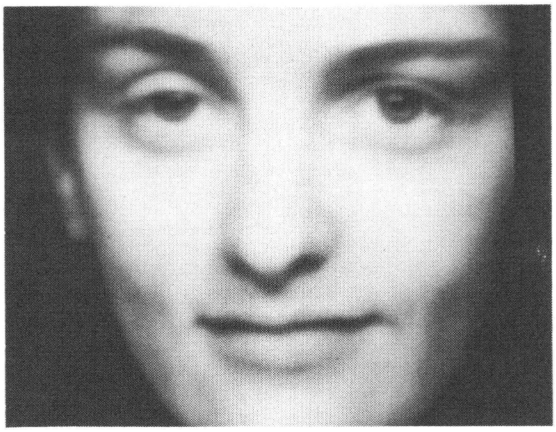

Fig. 3 Original image of face

Fig. 4 Gradient image of face showing gradient strength and direction

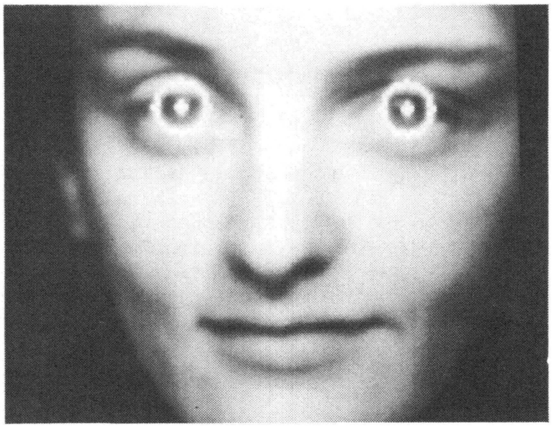

Fig. 5 Image of subject 3 showing detection of irises

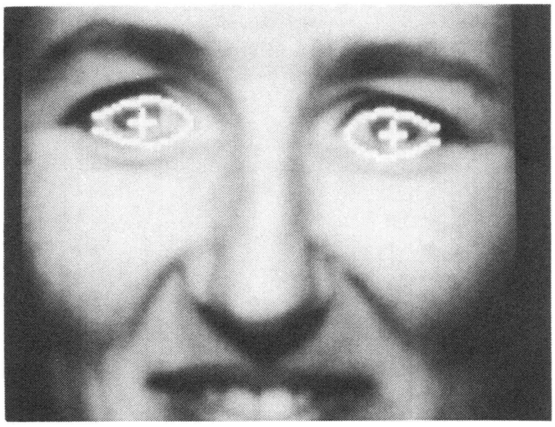

Fig. 6 Image of subject 6 showing detection of perimeter of sclera

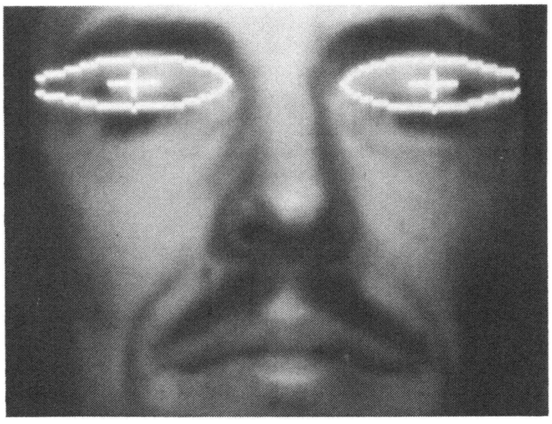

Fig. 7 Image of subject 1 showing detection of region below eyebrows

Research Report on “Efficient Blood Vessel Detection Algorithm For Retinal Images Using Local Entropy Thresholding”

Thitiporn Chanwimaluang and Guoliang Fan

School of Electrical and Computer Engineering
Oklahoma State University, Stillwater, OK 74078
Email: {thitipo,glfan}@okstate.edu

***Abstract*— An efficient algorithm for automated detection and extraction of blood vessels in retinal images has been presented in this paper. Especially the delineation of vascular intersections/ crossovers has also been described in this paper. The algorithm mentioned in this paper consists of four steps: matched filtering, local entropy thresholding, length filtering, and vascular intersection detection. Matched filtering is used for enhancing the blood vessels, Entropy based thresholding can keep the spatial structure of vascular tree segments well and Length filtering is used to remove misclassified pixels. Twenty ocular fundus images have been used for testing the proposed algorithm and experimental results are compared with those obtained from a state-of-the-art method and hand-labeled ground truth segmentations.**

Keywords—blood vessel detection, local entropy thresholding, image processing, matched filter, length filtering, retinal images

I. Introduction

Image processing is one of the key terms which is driving automation, security and safety related application of the electronic industry. Gigantic image processing solutions has become ever more complicated nowadays, but have served as an immense help for solving many problems in real time applications. Efficient Blood vessel detection has been one of such problems which fascinated researchers for several years. The automatic detection of blood vessels in retinal images can help doctors and physicians in diagnosing ocular diseases, patient screening, clinical study etc. The information extracted from retinal images can be used to identify the callousness of the patient’s condition. Information about pathological changes caused by some diseases including diabetes, hypertension and arteriosclerosis can be obtained from the appearance of blood vessels in the retinal images. Early detection through regular screenings is the most effective method for diagnosing eye related diseases. Additionally, vascular tree segmentation seems to be the most suitable method in the representation of the image registration applications due to the following reasons (1) it maps the whole retina (2) it does not move except in few diseases (3) it contains enough information for the localization of few anchor points.

Much study has been made in this field and several automated methods has been proposed to achieve this goal. An early attempt in this field was an edge detection based method [1], where the significant edges along the boundaries were extracted, since the local gradient maxima occur at these boundaries. Certain criteria set like opposite gradient direction and spatial proximity are set and the grouping process searches for the partner for each edge which satisfies these criteria. As far as tracking based method [2] is concerned, each vessel segment is defined by three attributes: direction, width and center point. Gaussian shaped function has been used to identify the density distribution of the cross section of blood vessels. An algorithm which keeps track of the center of the blood vessels and makes some predictions about the future path of the vessels based on vessel properties, is used to identify the individual segments. This method requires the manual selection of beginning and ending points using cursor. Matched filter response (MFR) image is used for mapping the vascular tree in the piecewise threshold probing technique [3]. A set of criteria is tested on the threshold of the probe region and the final decision whether the area being probed is a blood vessel or not is made. Different thresholds can be applied throughout the image for mapping blood vessels, since the MFR image is probed in a spatially adaptive way.

This paper proposes a new algorithm for efficiently locating and extracting blood vessels in ocular fundus images. The proposed algorithm consists of four steps: matched filtering, local entropy thresholding, length filtering, and vascular intersection detection. This algorithm does not involve any human intervention while comparing to paper [2] and requires less computational complexity while comparing to paper [3], since this algorithm automatically estimate one optimal threshold value.

II. Proposed Algorithm

The proposed algorithm consists of four steps. Matched filter has been applied to enhance the blood vessels with the generation of a MFR image, since the blood vessels usually have lower reflectance compared with the background. Secondly, an entropy based thresholding technique has been used to distinguish the vessel segments and background in the

MFR image. Misclassified pixels are removed using length filtering technique and vascular intersection detection has been performed by a window based probing process.

A. Matched Filter

A Gaussian shaped curve has been used to approximate the gray level profile of the cross section of a blood vessel in the method described in paper [4]. Piecewise linear segments of blood vessels can be can be detected from retinal images using the concept of matched filter detection. Usually, blood vessels have poor local contrast. In order to highlight the blood vessels, the two-dimensional matched filter kernel is designed to convolve with the original image. A prototype matched filter kernel is expressed as

$$f(x,y) = -\exp(-x^2/2\sigma^2), \text{ for } |y| \leq L/2 \qquad (1)$$

where L is the length of the segment for which the vessel is assumed to have a fixed orientation and the direction of the vessel is assumed to be aligned along the y-axis. The kernel needs to be rotated for all possible angles, because a vessel may be oriented at any angle. Convolution is done on the fundus image by a set of twelve 16x15 pixel kernels and at each pixel, only the maximum of their performance is retained. For example, Fig 2(a) shows the retinal image with low contrast between the blood vessels and the background and Fig 2b shows the MFR version, where the blood vessels are significantly highlighted or enhanced.

B. Local Entropy Thresholding

Extraction of vessel segments from the background is done by processing the MFR image using a proper thresholding scheme. An efficient entropy based thresholding algorithm which considers the spatial distribution of gray levels is used, since the image pixel intensities are not independent of each other. Particularly, a local entropy thresholding technique mentioned in paper [5] is implemented, since it can well preserve the spatial structures in binarized or thresholded image. Two images that have identical histograms but different spatial distribution will result in different entropy (also different threshold values).

The co-occurrence matrix of the image F is a PxQ dimensional matrix $T = [t_{ij}]_{P \times Q}$ gives an idea about the transition of intensities between the neighboring pixels, shows the spatial structural information about the image. Depending upon the ways in which the gray level i follows gray level j, different definitions of cooccurrence matrix are possible. The co-occurrence matrix is made asymmetric by considering the horizontally right and vertically lower transitions. Thus, t_{ij} is defined as follows:

$$t_{ij} = \sum_{l=1}^{P} \sum_{k=1}^{Q} ɗ \qquad (2)$$

where ɗ = 1, if f(l,k) = i and f(l,k+1) = j
or
if f(l,k) = i and f(l+1,k) = j
ɗ = 0, otherwise.

The probability of co-occurrence p_{ij} of gray levels i and j can therefore be written as

$$p_{ij} = t_{ij} / \sum_i \sum_j t_{ij} \qquad (3)$$

Is s, 0≤s≤L-1 is a threshold, then 's' can partition the co-occurrence matrix into 4 quadrants, namely A, B, C and D as shown in Fig 1.

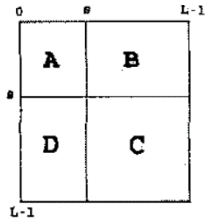

Figure 1: Quadrants of co-occurrence matrix [5].

Let us define the following quantities:

$$P_A = \sum_{i=0}^{s} \sum_{j=0}^{s} p_{ij}$$
$$P_C = \sum_{i=s+1}^{L-1} \sum_{j=s+1}^{L-1} p_{ij} \qquad (4)$$

The probabilities are normalized within each individual quadrant, such that the sum of the probabilities of each quadrant equals one, we get the following cell probabilities for different quadrants:

$$P_{ij}^{A} = \frac{p_{ij}}{P_A} = \frac{t_{ij} / (\sum_{i=0}^{L-1} t_{ij})}{\sum_{i=0}^{s} \sum_{j=0}^{s} t_{ij} / \sum_{i=0}^{L-1} \sum_{j=0}^{L-1} t_{ij}} = \frac{t_{ij}}{\sum_{i=0}^{s} \sum_{j=0}^{s} t_{ij}} \quad \text{for } 0 \leq i \leq s, 0 \leq j \leq s \qquad (5)$$

Similarly,

$$P_{ij}^{C} = \frac{p_{ij}}{P_C} = \frac{t_{ij}}{\sum_{i=s+1}^{L-1} \sum_{j=s+1}^{L-1} t_{ij}} \quad \text{for } s+1 \leq i \leq L-1, s+1 \leq j \leq L-1 \qquad (6)$$

The second entropy of the object can be defined as:

$$H_A^{(2)}(s) = -\frac{1}{2} \sum_{i=0}^{s} \sum_{j=0}^{s} P_{ij}^{A} \log_2 P_{ij}^{A} \qquad (7)$$

Similarly, the second entropy of the background can be defined as:

$$H_C^{(2)}(s) = -\frac{1}{2} \sum_{i=s+1}^{L-1} \sum_{j=s+1}^{L-1} P_{ij}^C \log_2 P_{ij}^C \qquad (8)$$

Hence, the total second-order local entropy of the object and the background can be written as:

$$H_T^{(2)}(s) = H_A^{(2)}(s) + H_C^{(2)}(s) \qquad (9)$$

Optimal threshold for object-background classification is obtained from the gray level corresponding to the maximum of $H_T^{(2)}(s)$. For the MFR image shown in Fig 2(b), the entropy based thresholding result is shown in Fig 2(c). Here we can notice that the blood vessels are clearly segmented from the background.

C. *Length Filtering*

We can see some misclassified pixels in image Fig 2(c). Our aim is to remove them and produce a clean and complete vascular tree structure. Length filtering is done to remove these isolated pixels and this is done using the concept of connected pixels labeling. Individual objects are represented using this connected region and we first need to recognize these separate connected regions. Isolation of these individual objects is done by length filtering using the eight-connected neighborhood and label propagation. Only the resulting classes exceed certain number of pixels, once the process is completed. Result after length filtering is shown in Fig 2(d).

D. *Detection of Vascular Intersections/Crossovers*

The most appropriate representation in registration process is the vascular intersections and crossovers, since they exist in every retinal image and do not move except some diseases. The branching points can be detected and characterized efficiently from the vascular tree, if it is one-pixel wide. The one pixel wide vascular tree is shown in Fig 2(e), and in order to obtain this, morphological thinning operation is applied. A 3x3 neighborhood window is used to probe and find the branching points for saving computational time. It is a branching point if the number of vascular tree in the window is greater than 3. Then a 11x11 neighborhood is applied through a detected branching points in order to eliminate small intersections [6]. We consider only the boundary pixels of a 11x11 square and is the number of vascular tree on the boundary is greater than 2, we mark it as an intersection/crossover. The vascular tree with intersections and crossovers is depicted in Fig 2(f).

III. SIMULATION RESULTS

The Computational time of this algorithm took approximately 3 minutes for each retinal image and the algorithm was tested on Windows XP, Pentium 4, CPU 1.7GHz using MATLAB version 6.1. The simulation results are compared with the state of art results obtained in paper [3] and hand-labeled ground truth segmentation shown in Fig 3, as part of evaluation of the performance of this algorithm.

The retinal images are specifically classified into three categories: normal retinal images, abnormal retinal images with some lesions and retinal images with obscure blood vessel appearance. In Fig 3, the first column shows results from normal retinal images, second column shows results from abnormal retinal images with some lesions and the third column shows results from retinal images with obscure blood vessel appearance. In Fig 3, the first row represents the original retinal images, second row represents the hand-labeled ground truth segmentations manually labeled by Hoover [3], and the third row represents the simulation results obtained using the algorithm in this paper. The algorithm mentioned in this paper can show a significant improvement in normal and obscure retinal images while comparing with the one in paper [3]. Extraction of blood vessels can be done better using this algorithm, for example, even the smaller blood vessels can be extracted. Matched filtering enhances the blood vessels against the background and Local entropy thresholding performs well in separating the enhanced blood vessels and the background since it considers the spatial distribution of gray levels and thus it can preserve the structural details of an image. The presence of lesions in abnormal retinal image is the major obstacle in extracting blood vessels, since they are also mistakenly detected as blood vessels. The algorithm in this paper is sensitive to the lesions because, tier boundaries partially match the shape of the matched filter kernels. While comparing, the algorithm in paper [3] is more robust towards lesions. The algorithm in this paper can be improved in robustness by including color information and additional anatomical constraints for blood vessel detection and extraction.

IV. CONCLUSION

An efficient algorithm for fully automated blood vessel detection in ocular fundus images using local entropy thresholding technique is introduced in this paper. The proposed algorithm has very less computational complexity and shows an accurate segmentation results in the case of normal retinal images and retinal images with obscure blood vessel appearance. Some lesions are mistakenly detected as blood vessels in the case of abnormal retinal images with some lesions. The robustness of the proposed algorithm can be improved in future by incorporating the pre-processing techniques and additional anatomical constraints to separate lesions from the final vascular tree.

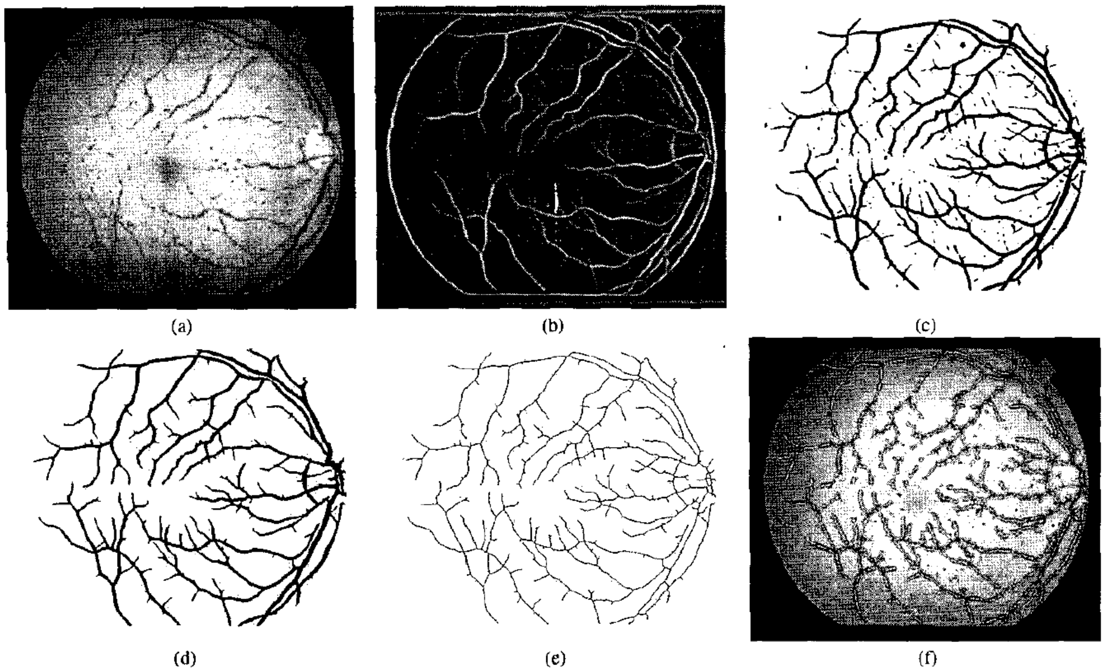

Figure 2: (a) An original retinal image. (b) Matched filtering result. (c) Local entropy thresholding result. (d) Vascular tree. (e) One-pixel wide vascular tree. (f) One-pixel wide vascular tree with intersections and crossovers overlaying on gray-scaled image.

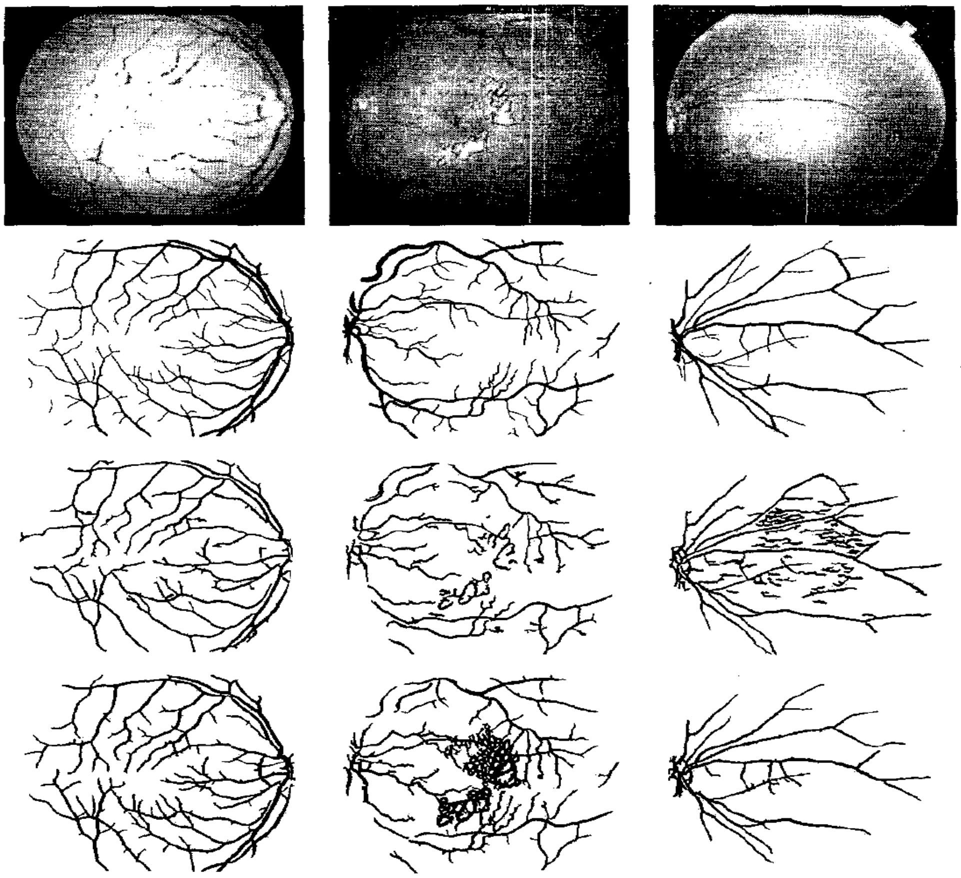

Figure 3: First row: Example images; Second row: Hand-labeled ground truth ([3]); Third row: Results from [3]; Last row: Results from our method.

V. References

[1] A Pinz. *S.* Bernogger. P. Datlinger. and A. Kruger, “Mapping the human retina:’ *IEEE Trans. Medical imaging*, vol. 17, no. 4, August 1998.

[2] L. Zhou, M. *S.* Rzeszotarski, L. Singeman, and I. M. Chokreff, “The detection and quantification of retinopathy using digital angiograms:’ *IEEE Trans. Medical imaging*, vol. 13, no. 4, December 1994.

[3] A Hoover, V. Kouznetsova, and M. Goldbaum. “Locating blood vessels in retinal images by piecewise threshold probing of a matched filter response,’’ *IEEE Trans. Medical imaging*, vol. 19, no. 3, March *2000*, http://www.ces.clemson.edu/ ahoover.

[4] *S.* Chaudhuri, S. Chatterjee, N. Katz, M. Nelson, and M. Goldbaum, “Detection of blood vessels in retinal images using two dimensional matched filters:’ *IEEE Trans. Medical imaging*, vol. 8, no. 3, September 1989.

[5] N. R. Pal and *S.* K. Pal, “Entropic thresholding,” *Signal processing.* vol. 16, pp. 97-108, 1989.

[6] A Can, H. Shen, J. N. Turner, H. L. Tanenbaum, and B. Roysam, “Rapid automated tracing and feature extraction from retinal fundus images using direct exploratory algorithms,” *IEEE Trans. Information Technology in Biomedicine*, vol. 3, no. 2, June 1999.

<u>Research Report</u>

Retinal thickness measurements obtained with Cirrus optical coherence tomography

Original Authors: P A Keane, P S Mand, S Liakopoulos, A C Walsh, S R Sadda

Research Report by: Vidya Viswanathan

Abstract

Aim: To analyze and find out the rigorousness and frequency of retinal thickness measurement errors in a Fourier domain optical coherence tomography (FDOCT) device, Cirrus OCT.

Methods: Data collection was done from 209 patients undergoing Cirrus OCT imaging with the Macular probe protocol. The exact position of the automated retinal edges used by Cirrus OCT software was examined using a 6-point scale. This software was used for measuring the thickness. Retinal morphological characteristics and disease diagnosis are some of the parameters which are correlated with the errors present.

Results: Retinal boundary detection was done in almost most of the data successfully and found that errors were observed in 57.5% of eyes, but were severe in only 9.6% of eyes. The recognition of sub retinal fluid, sub retinal tissue, pigment epithelium detachment or a diagnosis of choroidal neovascularization was concerned with more severe errors, at the same time, the presence of retinal cysts or a diagnosis of retinal vascular disease were less likely to be associated with significant error.

Conclusions: The presence of errors in the measurement of retinal thickness happened less frequently with Fourier domain OCT (Cirrus OCT). Segmentation errors were the major concern especially in the examination of eyes with structurally complex retinal disease. Examining the segmentation errors may be a crucial factor in determining the relative merits of the system, with the recent release of multiple FDOCT systems.

Keywords—retinal thickness detection, cirrus optical coherence tomography, image processing, retinal images.

I. INTRODUCTION

Background and Significance: Image processing is one of the key terms which is driving automation, security and safety related application of the electronic industry. Gigantic image processing solutions has become ever more complicated nowadays, but have served as an immense help for solving many problems in real time applications. Retinal thickness measurement has been one of such problems which fascinated researchers for several years. Macular oedema has been found as the common cause for reduced vision in patients with retinal vascular disorders such as diabetic retinopathy.

Prior work and Content of innovation: The extent of macular thickening was identified clinically or with stereoscopic fundus photography methods in the past. These methods permit semi quantitative assessment at its best. The introduction of optical coherence tomography in the recent period has changed drastically, the control of vitreoretinal disease. Especially, the high axial resolution offered by OCT is very much suitable for the accurate examination of macular oedema. Apart from these, OCT has been extra ordinary in its ventures to detect retinal thickness from image data in an objective and automated manner.

The most popular OCT system, Stratus OCT uses image processing techniques to automatically recognize the inner and outer retinal edges on OCT B-scans (segmentation) and thus provides results of retinal depth measurements. Recognition of retinal thickness is possible at multiple positions using these techniques and also to construct retinal thickness maps. However, care is needed in the use of these techniques, as there are chances for errors to occur in the retinal segmentation. Errors in retinal thickness measurements may be observed in 92% of eyes imaged with Stratus OCT and severe measurement errors were found in 13% of eyes, as demonstrated by the earlier attempts. Other reports have confirmed these findings and suggest that segmentation errors happen more often in macular disorders with complex morphology like neovascular age related vascular degeneration (AMD).

Latest technological improvements made the speed of OCT systems to be incremented by many orders of magnitude. Improvements in the light sources used by OCT has given way to increase in image resolution. Many OCT systems which involve these improvements have been recently introduced to the ophthalmic market-these systems are commonly called as spectral domain or Fourier domain optical coherence tomography (FDOCT). With Stratus OCT, this apparatus includes image analysis software that provides calculation of retinal thickness and may be subjected to same segmentation problems. However, the speed and image resolution advantages of FDOCT and improvements in image processing may advance the accuracy of retinal segmentation.

Key Contributions: In this paper, we tried a systematic assessment of both the frequency and rigorousness of segmentation errors in a recently introduced FDOCT successor to the Stratus OCT, the Cirrus OCT.

II. MATERIALS AND METHODS

A. Flow Chart showing the methodology

The diagram showing the methodology followed in this paper is shown in Figure A.

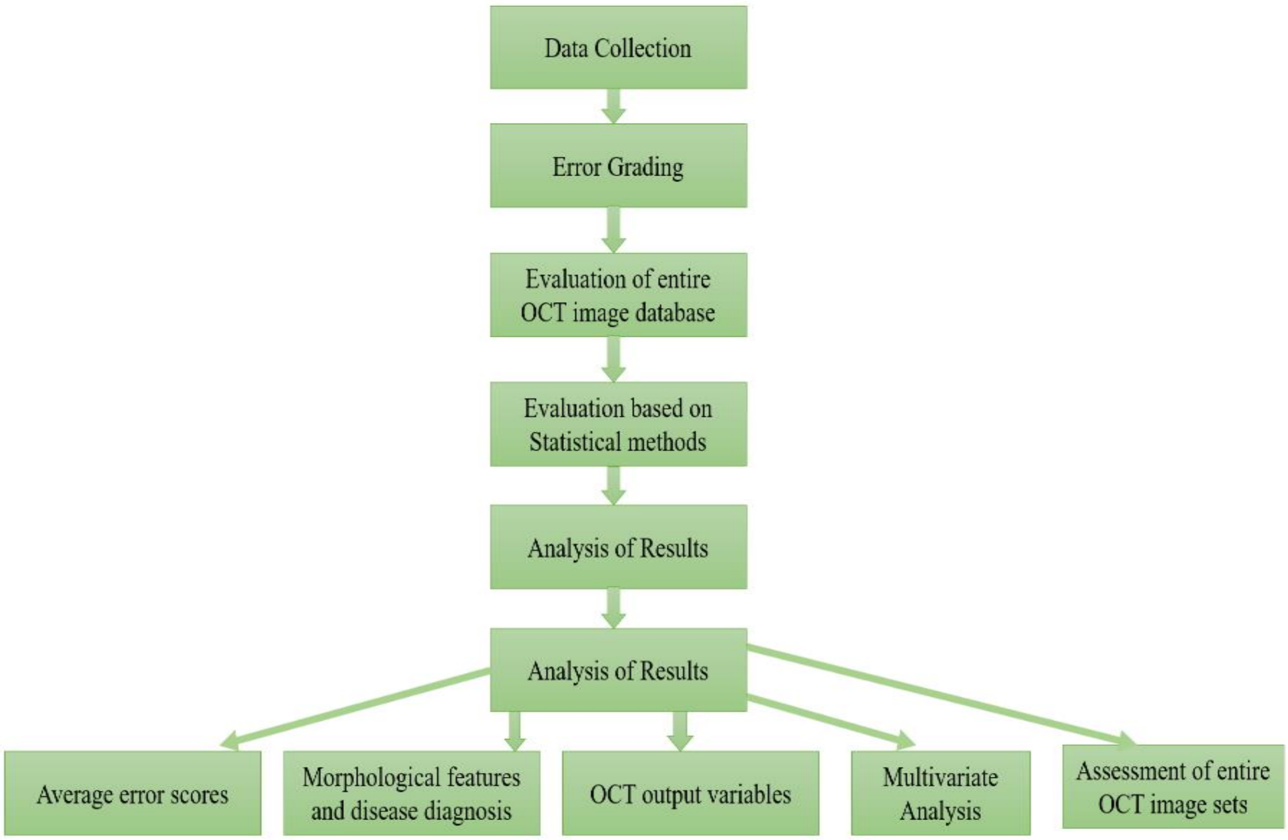

Figure A: Flow chart demonstrating the steps in methodology

B. Data Collection

As a part of data collection for this project, 209 consecutive patients with OCT imaging were selected from an alphabetical list from the Cirrus OCT database at the Doheny Eye Institute, Los Angeles, USA. In order to recognize the primary eye for which the imaging test was requested, the clinical records were reviewed for each patient and this eye was selected for the analysis in the study. In cases where the imaging was requested for both the eyes and the primary eye was not located, the eye used for study was chosen randomly using a random number generator. For those patients who took the tests at multiple dates, the first available image from the dataset were chosen. All these scans were obtained between January 19, 2008 and October 10, 2008.

Macular cube or the 5 Line Raster scanning protocols were used for obtaining the Cirrus OCT macular images. Identification of the inner and outer retinal edges and the macular depth calculations are done using Macular Cube protocol, while the high-quality 5 Line Raster protocol is used especially for qualitative evaluations. The 5-line raster protocol includes a horizontal scan through the foveal center, with two further horizontal scans on each side. Each line is 6 mm in length and separated by 250 mm, so that together the five lines cover 1 mm in height and span the foveal central subfield. The 128 OCT B-scans were collected by the Macular Cube protocol in a consecutive and automated fashion. Each of the 128 B-scans is composed of 512 equally spaced transverse sampled locations. Five scans, chosen to correspond with the location of each of the high-definition 5 Line Raster scans, were selected from each 128 B-scan stack for analysis. There are many advantages obtained for choosing this limited set of B-Scans: (1) Helps in examining error rigorousness (2) It focuses the evaluation on scans near the fovea which are more often to be affected by pathology and more clinically relevant (3) It allows a more compatible comparison with the prior study examining errors in Stratus OCT in which all radial B-scans pass through the foveal central subfield. Cirrus OCT version 3.0.0.64 software was used for doing the thickness measurement analysis. Experienced photographers who have been certified for OCT scan capture by image reading centers for clinical studies took all the scans used for this study.

C. Grading of errors

Each of the 5 cross sectional images were reviewed systematically by a certified grader (PAK) at the Doheny Image Reading Center, after a single eye was selected for each patient in the chosen database. The obtained position of the automated inner and outer retinal edge segmentation lines with respect to the exact position of the boundaries was scrutinized at every A-scan position along each B-scan. The grader was able to show or hide the automated boundary lines as needed, to complete the assessment using the Cirrus OCT machine. The presence and severity of errors in boundary detection for each of the five images were graded according to the previously published cumulative points scale: one point was given for any error (defined as the deviation of a line from the actual edge) (2) one point was given for any error within 500 micrometers of the foveal center (corresponding to the foveal subfield; the rationale for assigning this point was to provide more weight to deviations that affect the foveal measurements that are used most commonly in clinical studies); (3) one point was given if the length of the edge error in the transverse dimension (or the sum of the transverse lengths in the case of multiple discontinuous errors) was more than 1 mm, and one additional point was given if the error was more than 3 mm (this takes information regarding the transverse extent of the boundary error); and (4) one point was given for a boundary error that resulted a deviation that was more than one-third of the exact retinal thickness, and an additional point was given if the error was more than two-thirds of the exact retinal thickness. The errors in both the inner and outer retinal boundaries were summed up mentally to evaluate the rigorousness or severity of the axial or transverse error.

Each line scan was given an error score which ranges from 0 to 6, using this semi quantitative scale, where 0 means no error. Error grading was performed prior to collection of other scan and patient specific data for analysis to minimize the bias. Signal strength, an image quality related parameter, signal to noise ratio of the instrument were recorded for each of the image sets. The presence of retinal cysts, intra retinal reflections, sub retinal fluid, sub retinal tissue, pigment epithelium detachment (PED) and epiretinal membranes was also noticed. The foveal central subfield thickness was also noted. Finally, all patients with a diagnosis of choroidal neovascularization (eg neovascular AMD, pathological myopia) or retinal vascular disease (eg diabetic retinopathy, venous occlusive disease) were noted down.

D. *Assessment of entire OCT image sets*

A simplified analysis was done on the selected 128 B-scans in the Macular Cube, apart from the detailed assessment described above. This analysis used an algorithm like the one mentioned in Ahlers et al. The OCT database was classified based on the frequency and severity of the errors present: Table A shows the category name and their definition in detail. Cube.

Category Name	**Definition or Possibilities**
Limited	• Presence of severe segmentation errors (>50% of retinal thickness) in more than 25 B-scans. • Presence of moderate segmentation errors (>20% of retinal thickness) in more than 50 B-scans.
Reasonable but significant errors	• At least one rigorous segmentation error (but less than 25). • At least five moderate segmentation errors (but less than 50)
Reasonable with negligible errors	• Less than five moderate segmentation errors
Perfect without segmentation errors	• No segmentation errors across the entire Macular Cube.

Table A: Classification of OCT data sets based on severity and frequency of errors present

E. *Statistical Methods*

Average Error Score shortly called as AES was calculated for each eye by finding the mean of the error scores of the 5 Cirrus OCT B-scans analyzed for each eye. This AES value considering both the inner and outer retinal edge separation, comprised of the primary dependent variable for all analyses. Apart from this, the AES was calculated separately for inner and outer retinal edges. As a part of qualitative assessment and classification, the AES values are divided in to three categories and it is shown in Table B.

Category Name	**AES level**
Mild	AES ≤ 2
Moderate	AES > 2 and AES ≤ 2
Severe	AES > 4

Table B: Qualitative Classification based on average error score

The mean, standard deviation and median AES were recorded for each category. The Wilcoxon rank sum test was used to examine whether the dependent variable, AES, were different between each level. The correlation with the AES was calculated using a Spearman correlation coefficient, in case of continuous variables, where as some continuous variables are divided in to categories for analysis. Example for such continuous variables are signal strength and foveal central subfield thickness. This extra experimentation was done to evaluate the potential thresholds that could be of use to doctors for recognizing eyes with a higher likelihood of erroneous scans. Population was divided into smaller number of cases/groups and to explore previous cutoff points used by reading centers as minimum standard of acceptability, signal strength category was chosen arbitrarily. In order to imitate the concepts of no oedema, sub clinical oedema and definite oedema, foveal central subfield categories were chosen. The parameters were taken for univariate and multivariate analysis in such a way that, all those parameters which had at least 0.10 level in the univariate analysis were involved in the multivariate analysis also. Models of independently predictive variables for AES was got using stepwise regression. The importance of each variable in improving the overall model was evaluated using Improvement

Chi square analysis. Variables should reach the level <0.10 to be present in the model. Recognition of most highly predictive model was done.

Commercially available software (Intercooled Stata for Windows, Version 9, Statacorp LP, College Station, Texas) was used for all statistical analysis. The accepted level of significance or all examinations was $p \leq 0.05$.

III. Results

A. *Average error scores*

The detailed version of AES results is given in table 1 in the paper. 57.5% of eyes were found to have retinal thickness measurement errors (29.2% mild, 18.7% moderate, 9.6% severe). The mean AES for the study population was 1.35, with a median of 0.60, mentioning as small error overall by this recognition system. The mean AES for the inner retinal edge alone (AES-inner) in isolation was 0.55 with (median 0.00), while that of the outer retinal edge (AES-outer) was 0.83 (median=0.00). These details are given in Table C below.

Percentage error of retinal thickness measurement	57.5% with: • 29.2% mild • 18.7% moderate • 9.6% severe
Study Population	• Mean AES: 1.35 • Median: 0.60
Inner retinal edge	• Mean AES: 0.55 • Median: 0.00
Outer retinal edge	• Mean AES: 0.83 • Median: 0.00

Table C: Overall results of Average Error Scores (AES)

B. *Morphological features and disease diagnosis*

The presence of sub retinal fluid, sub retinal tissue or PED was related with significantly higher mean AES, with scores of 2.63, 2.81 and 1.9, respectively. This is given in figure 2 in the paper. The presence of an ERM was also related with significantly higher mean AES, with a score of 2.03. The presence of retinal cysts and intra retinal hyper-reflective structures (usually lipid exudates) did not show a meaningful relationship with mean AES. The detailed version of results is given in table 2 in the paper.

Disease detection was also concerned with the rigorousness of retinal thickness calculation errors. A higher mean AES was exhibited by eyes with choroidal neo vascularization, whereas eyes with retinal vascular disease (such as macular oedema from diabetic retinopathy) had significantly lower mean error scores (table 1 in the paper).

C. *Optical coherence tomography output variables*

47.8% of the eyes evaluated had a mean AES of 1.03 with a signal strength of 10. Higher mean AES scores of 1.64 ($p=0.0018$) was obtained by eyes having signal strength less than 10 (52.2%). Signal strength less than or equal to 5 have been showed by 13 eyes. Eyes having foveal central subfield thickness less than or equal to 200, or greater than 300, had significantly higher mean AES scores than those with FCS thickness of 201–300 ($p=0.0001$) (table 1 in the paper).

Signal strength was importantly and negatively related with the AES ($r=-0.1894$; $p=0.006$) in case of continuous variables. This shows more severe measurement errors were occurred for lower signal strength. A modest and statistically important correlation with increased AES ($r = 0.3321$; $p<0.0001$) was obtained by increasing foveal central subfield thickness.

D. *Multivariate analysis*

Table 3 in the paper shows the findings of multivariate analysis. A reduced signal strength and the existence of sub retinal fluid, epiretinal membrane or sub retinal tissue were found to be independently predictive, accounting for 36% of the variability in the AES, in the most highly predictive model.

E. *Assessment of entire OCT image sets*

Table D shows the retinal boundary segmentation classification with the percentage of eyes belonging to each of the categories after examining the 128 OCT B-scans got with the Macular Cube protocol. Detection of choroidal neo vascular disease was concerned with increasing severity of segmentation error ($p=0.006$), using this categorization. There is no statistically important relationship between retinal vascular disease recognition and increasing rigorousness of segmentation error ($p=0.714$).

Category Name	**Percentage of eye images belongs**
Limited	14.4%
Reasonable but significant errors	33.1%
Reasonable with negligible errors	10%
Perfect without segmentation errors	42.3%

Table D: Percentage of eyes belongs to each category

IV. OVERALL REVIEW AND DISCUSSION ON LIMITING CONDITIONS

This report states that errors in retinal thickness measurement provided by Cirrus OCT were usual with a minimum error happening in 57% of image sets. Errors in retinal thickness calculation occurred in 92% of patients imaged with Stratus OCT in the earlier study with the same algorithm and using a similar patient population. Improvements can be done in OCT image quality by increasing speed, resolution and sensitivity of Cirrus FDOCT. Automatic alignment of A-scans, using image-processing techniques, is needed to remunerate for motion artefacts and, thus, to make sure the perfect edge identification, due to the slow speed of Stratus OCT. This function is not needed in FDOCT systems, as the high-speed scanning of these instruments enhances or improves the problem of A-scan disarrangement. Improved signal-to-noise ratios are obtained by increasing sensitivity of FDOCT, thus decreasing the effect of media opacities such as cataract. Improved visualization of retinal structures is obtained by the greater axial resolution of FDOCT, which may give way to improvements in the efficacy of segmentation algorithms.

Reduced error rate in Cirrus OCT quantitative analysis is obtained by improvements in computer image-processing techniques and segmentation algorithms. Ahlers et al have pointed out the concepts underlying image segmentation in Cirrus OCT software, even though the exact details are private. Cirrus OCT locates the outer boundary of the retina at the anterior border of the retinal pigment epithelium (RPE), whereas Stratus OCT has the possibility of wrongly choosing the inner segment–outer segment (IS–OS) junction of the photoreceptors as the outer edge of the retina. Even though the RPE may be damaged in disorders such as choroidal neovascularization, the choice of this edge is likely to lead to more robust segmentation than the IS–OS junction.

Cirrus OCT image sets containing intra retinal cystoid space, or focal areas of intra retinal hyper-reflectivity persistent with lipid discharge, were not related with increased average error scores, in this report. Withal, patients categorized as having retinal vascular diseases (eg, diabetic macular oedema), were not more prone to have increased error scores. Analyzing the results from Stratus OCT, it is clear that the finding is uniform and suggests that automated retinal depth calculations obtained from Cirrus OCT may be perfect enough for embodiment in clinical trials of these disorders. Regarding the manual correction of segmentation errors in Stratus OCT image sets obtained from patients with diabetic macular oedema, even large study from the Diabetic Retinopathy Clinical Research Network did not find any supplementary benefit and the study observations and conclusions were not impaired by the corrected results.

Cirrus OCT images showing the features of sub retinal tissue, PED or sub retinal fluid were related with notably increased average error scores. Moreover, eyes with choroidal neo vascular diseases, such as neo vascular AMD, were found to have increased error scores. 9.6% of the Cirrus OCT image sets were found to have average error scores in the extreme range and 13% of Stratus OCT image sets were earlier shown to have severe errors—in both cases, severe errors happened widely as a result of the complex morphology in choroidal neo vascular disease. Many other studies using Stratus OCT have demonstrated that segmentation errors happen more periodically and with higher rigorousness in diseases such as neo vascular AMD. Manual segmentation of the boundaries may be obligatory for accurate measurement until, improvements in image analysis software allows accurate picture of the inner and outer retinal boundaries in patients with complex retinal disease. Undoubtedly, this issue has been addressed in the latest versions of Stratus and Cirrus OCT software, which permits manual correction of incorrectly positioned boundaries.

Cirrus OCT images indicating proof of epiretinal membrane formation was also related with errors in inner retinal boundary recognition, in many cases giving way to overestimation of foveal central subfield thickness, or average retinal thickness over a wide retinal area. Qualitative assessment of the vitreoretinal interface using dense OCT datasets is generally used to estimate the appropriate time for surgical intervention in these patients. Nonetheless, caution should be operated in the interpretation of changes in retinal thickness following surgical intervention for these conditions, as a result of inner retinal boundary segmentation errors.

It has been clear from the experimentation that, our study has a number of advantages, especially a nearly large sample size, and the use of a standard OCT image acquisition protocol by certified ophthalmic photographers. Further, a standardized categorical scale for error assessment permitted estimation of error severity and facilitated direct comparison with our earlier study. The relative weights of the various components remain arbitrary determinations, while the categorical scale utilized in this study allows us to rate the severity of segmentation errors by Cirrus OCT, and to give additional weight to errors affecting the foveal center. Furthermore, a quantitative evaluation of the magnitude of retinal thickness errors is not feasible using this algorithm. This work may also be criticized for its emphasis on evaluation of segmentation in the foveal central subfield. As a solution for this problem, we did a supplementary, simplified, analysis of retinal boundary segmentation across the entire 128 B-scans of each image set. Other limitations comprise the retrospective nature of the study and the fact that separation efficacy was only evaluated on an FDOCT system from a single vendor. At last, we can say that, Cirrus OCT software permits for identification of an additional boundary not evaluated in this study: ‘‘RPE-fit.’’ In cases of PED, the image-analysis software attempts to portray the estimated normal position of the RPE using RPE-fit, thus leading to quantification of the PED. Regarding future studies for specific disorders such as neo vascular AMD, Evaluation of RPE-fit segmentation may be of great value.

V. COMPARATATIVE STUDY ON OTHER METHODS

As a part of comparative study with other algorithms, many innovative and fascinating works were reviewed and analyzed on the field of retinal thickness measurement using optical coherence tomography. A.Chan [2] worked on recording normal macular thickness measurements in healthy eyes using a commercially available latest software, which is the optical coherence tomography mapping software version 3.0 from the Stratus OCT. They conducted an ophthalmic evaluation involving OCT, on 37 different eyes from thirty-seven healthy people. They acquired six radial scans of 6mm in length and centered on the fovea using OCT3. Automatic computation of retinal thickness was done using the mapping software and the measurements were demonstrated as the mean and standard deviation every region defined in the Early Treatment Diabetic Retinopathy Study (ETDRS). The results show that the foveal thickness, which is the mean thickness in the central 1000-µm diameter area and central foveal thickness, which is the mean thickness at the point of intersection of 6 radial scans on OCT3 were 212±20 and 182±23µm, correspondingly. Experiments show that macular thickness measurements were smallest at the center of the fovea, largest within 3-mm diameter of the center, and declined toward the periphery of the macula. The nasal quadrant was thicker than the temporal quadrant. Manual determination of Central foveal thickness was done and it was found to be 170±18µm, roughly 12µm less than the value automatically obtained from the OCT3 software. Findings also proves that there is no relationship between foveal thickness and age. Average foveal depth calculations were 38 to 62µm thicker than earlier recorded values, while mean central foveal thickness measurements were 20 to 49µm thicker than already published values. This divergence must be taken into account while analyzing OCT scans.

A comparative study of retinal thickness in normal eyes using stratus and spectralis optical coherence tomography was demonstrated in S. Grover [3]. Spectral domain OCT (SDOCT) is an improvement of time domain OCT (TD-OCT) in the diagnosis of retinal diseases. Retinal thickness measurements differ in both the cases, due to the difference in the outline of the outer edge of the retina differs in both the instruments. The main objective of this study is to assess this divergence by the juxtaposition of macular thickness got from Stratus and Spectralis OCT. This study was conducted only on those retinal images without any known retinal disease. 36 subjects with no history of retina related disorders and with normal vision and normal intraocular pressure were chosen for evaluation. Stratus as well as Spectralis OCT imaging was done on these subjects on one eye, by the same operator. Measurement of Central point thickness (CPT) and retinal thickness in nine ETDRS subfields, including central subfield (CSF) was done. Statistical significance was determined using Student's *t*-test. The study proved that retinal thickness measurement was high when measured using Spectralis OCT compared to the Stratus OCT and the value was approximately 65 to 70 µm. This is due to the inclusion of the outer segment-RPE-Bruch's membrane complex by Spectralis OCT, which is relevant to studies using the latest SD-OCT for evaluation of retinal depth.

A comparative study and interchangeability of macular thickness measured with Cirrus OCT and Stratus OCT in myopic Eyes was mentioned in G. Wang [3]. The main objective of their study was to explore the disparity of macular thickness between the Stratus OCT and the Cirrus OCT and to formulate a conversion formula to interchange the thickness measurements possessed using these two devices. As a part of the study, they chose a myopic patient for their research. Experiments were conducted on eighty-nine healthy Chinese adults with spherical equivalent ranging from -1.13 D to -9.63 D diameters. Both the Stratus OCT and Cirrus OCT was used to measure the macular thickness and the interdependence between macular thickness and axial length as well as the compatibility between the two OCT measurements were examined. An equation was developed to swap the macular thickness acquired using bothe OCT instruments. Results show that there was no statistically important relationship between axial length and central subfield macular thickness measured with both Stratus OCT and Cirrus OCT. The formula $(CMT)_{\text{Cirrus OCT}} = 78.328+0.874 \text{ x}(CMT)_{\text{Stratus OCT}}$ was developed to interchange macular thickness acquired with two OCT instruments. Study concluded that macular thickness calculated in myopic eyes using Cirrus OCT were thicker than that of Stratus OCT. The formula mentioned above can be used to interchange the thickness measurements using both instruments. Improving the developments and future directions must include studies with diverse OCT instruments and larger databases to enable the comparison of macular thickness measurements with different OCT appliances.

VI. CONCLUSION

Method/Data based conclusions: Affirmation proving that automated segmentation errors happen less frequently in the latest or recently introduced FD Cirrus OCT system.

Limiting Conditions: Segmentation error will be a problem for the quantitative evaluation of retinal disorders with complex morphological features, like choroidal neovascularization.

Future works/Direction for further research: More literature review is needed to conduct a comparative study regarding the frequency and severity of segmentation errors. They occur across the range of recently introduced FDOCT systems. Measurement of this factor may be crucial in identifying the relative advantages of these devices.

VII. REFERENCES

[1] P A Keane, P S Mand, S Liakopoulos, A C Walsh, S R Sadda. *"Accuracy on retinal thickness measurements obtained with Cirrus optical coherence tomography";* Br J Ophthalmol 2009 93;1461-1467; July 1, 2009.

[2] *Annie Chan, MD; Jay S. Duker, MD; Tony H. Ko, PhD; James G. Fujimoto, PhD; Joel S. Schuman, MD. "*Normal Macular Thickness Measurements in Healthy Eyes Using Stratus Optical Coherence Tomography".

[3] *Sandeep Grover, Ravi K. Murthy, Vikram S. Brar, and Kakarla V. Chalam. "*Comparison of Retinal Thickness in Normal Eyes Using Stratus and Spectralis Optical Coherence Tomography".

[4] Geng Wang, Kun-Liang Qiu, Xue-Hui Lu, Ming-Zhi Zang. "Comparison and interchangeability of macular thickness measured with Cirrus OCT and Stratus OCT in myopic eyes".

<u>Research Report - 4</u>

[Paper 3]

Review on the impact of CT scanning parameters on volumetric measurements of pulmonary nodules by 3D active contour segmentation

Research Report by:

Vidya Viswanathan
MSEE Graduate Student
University of Washington
Bothell, WA

Abstract

Aim: The major goal of this research is to explore the impact of CT scanning and recreation parameters on computerized sectioning and volumetric computation of nodules in computed tomography images.

Methods: Phantom nodules of known sizes were utilized so that division exactness could be measured in contrast with ground-truth volumes. Circular nodules having 4.8, 9.5, and 16 mm distances across and 50 and 100 mg/cc calcium substance were implanted in lung-tissue simulating foam which was embedded in the thoracic cavity of a chest segment phantom. CT scans of the phantom were obtained with a 16-cut scanner at different tube currents, pitches, fields-of-view, cut interims, and cut thicknesses. Scans were likewise taken utilizing indistinguishable procedures either around the same time or five months separated for investigation of reproducibility. The phantom knobs were sectioned with a 3-dimensional active contour (3DAC) model that we already produced for use on patient nodules. The rate volume blunders in respect to the ground-truth volumes were evaluated under the different imaging conditions.

Results: There was no factually critical distinction in volume error for rehashed CT scans or scans brought with methods where just pitch, field-of-view, or tube current (mA) was changed. Be that as it may, cut thickness essentially ($p < 0.05$) influenced volume error. In this manner, to assess nodule development, reliable imaging conditions and high determination ought to be utilized for obtaining of the serial CT filters, particularly for littler nodules.

Conclusions: Understanding the impacts of scanning and remaking parameters on volume estimations by 3DAC permits better elucidation of information and evaluation of development. Following nodule development with electronic division techniques would decrease inter and intra observer fluctuations.

Keywords—lung nodule, sectioning, volume measurement, phantom study, CT scan.

I. Introduction

Background and Significance:

Image processing is one of the key terms which is driving automation, security and safety related application of the electronic industry. Gigantic image processing solutions has become ever more complicated nowadays, but have served as an immense help for solving many problems in real time applications. Computed tomography scanning has been one of such problems which fascinated researchers for several years. Computed tomography (CT) is touchier than chest radiography in identifying little and unobtrusive lung knobs. With the approach of multi-indicator row helical CT scanners that offer ever more slender cuts, significantly more knobs are identified. As it is prescribed to catch up on most, if not every single distinguished knob, the administration of these knobs may overpower radiologists, particularly if lung tumor screening with CT progresses toward becoming suggested practice.

Prior work and Content of innovation:

Computer-aided diagnosis (CAD) devices can possibly help radiologists as a second reader in recognizing, arranging (describing), and overseeing lung knobs. Presently, a Computer aided design framework can break down a single scan, dividing and acquiring characteristics from the nodule to gauge its probability of threat. Elements, for example, morphology (volume, size and shape), histograms of graylevels, the difference of the nodule, improvement after differentiation infusion, and surface have been utilized. There has additionally been expanding consideration given to volume multiplying rate as a pointer of danger.

To track volume development, an exact limit of the knob is required, and it is difficult for many reasons. To start with, it is hard to decide knob limits conclusively, as proposed by the inter and intra-spectator inconstancies among radiologists in surveying lung knob measure. Second, the strategy used to quantify volume may differ. Nodule size must be measured in two measurements on a CT cut, commonly in light of its longest and perpendicular axis. It is hard to evaluate multiplying time, particularly for littler knobs, for which a little change in diameter compares to a vast change in the volume. For instance, a sphere with a 3 mm diameter doubles in volume when the diameter increments by just 26% to 3.78 mm. This 0.78 mm increment is about the extent of 1.1 pixels in a typical scan with a field-of-view (FOV) of 36 cm.

Distinctive window width and level settings can likewise influence the estimation of diameters (Harris et al., 1993). These elements add to errors in the deliberate volume (Winer-Muram et al., 2003), bringing about irregularity and vulnerability in recognizing volume change in serial CT checks. The substantial inter and intra- spectator variations in radiologists' manual division exhibited in the 23 knobs given by the Lung Image Database Consortium (LIDC) highlight the trouble in judgment of knob limits on CT scans (Meyer et al., 2006). Yankelevitz et al. found that mechanized techniques are exact on phantom nodules and connected the strategies to clinical patient scans after some time. They inferred that automated techniques utilizing CT volumetric data that are not influenced by windowing settings or intra-and inter observer errors will be helpful for knob volume estimation and for surveying development (Yankelevitz et al., 1999; Yankelevitz et al., 2000).

Despite the fact that modernized techniques might be resistant to a few elements that may impact radiologists, for example, variety in windowing, there are still difficulties because of image procurement parameters (Zerhouni et al., 1982; Im et al., 1988). Different groups have explored the impacts of image procurement parameters utilizing knob emulating spheres with known volumes. Ko et al. revealed PC computed volumes from region of interest (ROI's) set apart by radiologists. Utilizing a threshold technique for division, they found that tube current-time (20 and 120 mAs), remaking calculation, quantitative strategy, nodule attenuation (solid at 50 HU and ground-glass at −360 HU), and nodule estimate fundamentally influenced volume error (Ko et al., 2003). Goo et al. measured volumes utilizing a thresholding technique and detailed that area thickness and edge altogether influenced absolute volume error (Goo et al., 2005).

Key Contributions:

The real contrasts between this examination and past reviews (Harris et al., 1993; Ko et al., 2003; Winer-Muram et al., 2003; Goo et al., 2005) incorporate the division algorithm, the more noteworthy scopes of scanning and reconstruction parameters and nodule sizes, and the impact of calcium concentration of the nodules. Likewise, we examined the reproducibility of rehashed scans performed either sequentially or isolated by a couple of months (five in this review) as in clinical follow-up studies. A robotized knob division strategy was utilized so the volume errors were surveyed free of inter and intra-observer variabilities.

Albeit phantom nodules are not the same as genuine pulmonary nodules from various perspectives, phantom studies will permit correlation with the ground-truth volumes and methodical examination of the relative patterns of the volume errors reliance on CT imaging conditions. This would be basically difficult to perform with nodules in patient scans. Other than dosage concerns, motion artifacts can be a noteworthy variable, making it hard to figure out what really adds to the deliberate volume errors. Notwithstanding the way that the total volume errors assessed with phantoms won't be relevant to genuine nodules, the outcomes will give helpful data to the determination of CT imaging conventions for clinical development and for the elucidation of nodule volume changes.

II. Materials and Methods

A. Flow Chart showing the methodology

The diagram showing the methodology followed in this paper is shown in Figure A.

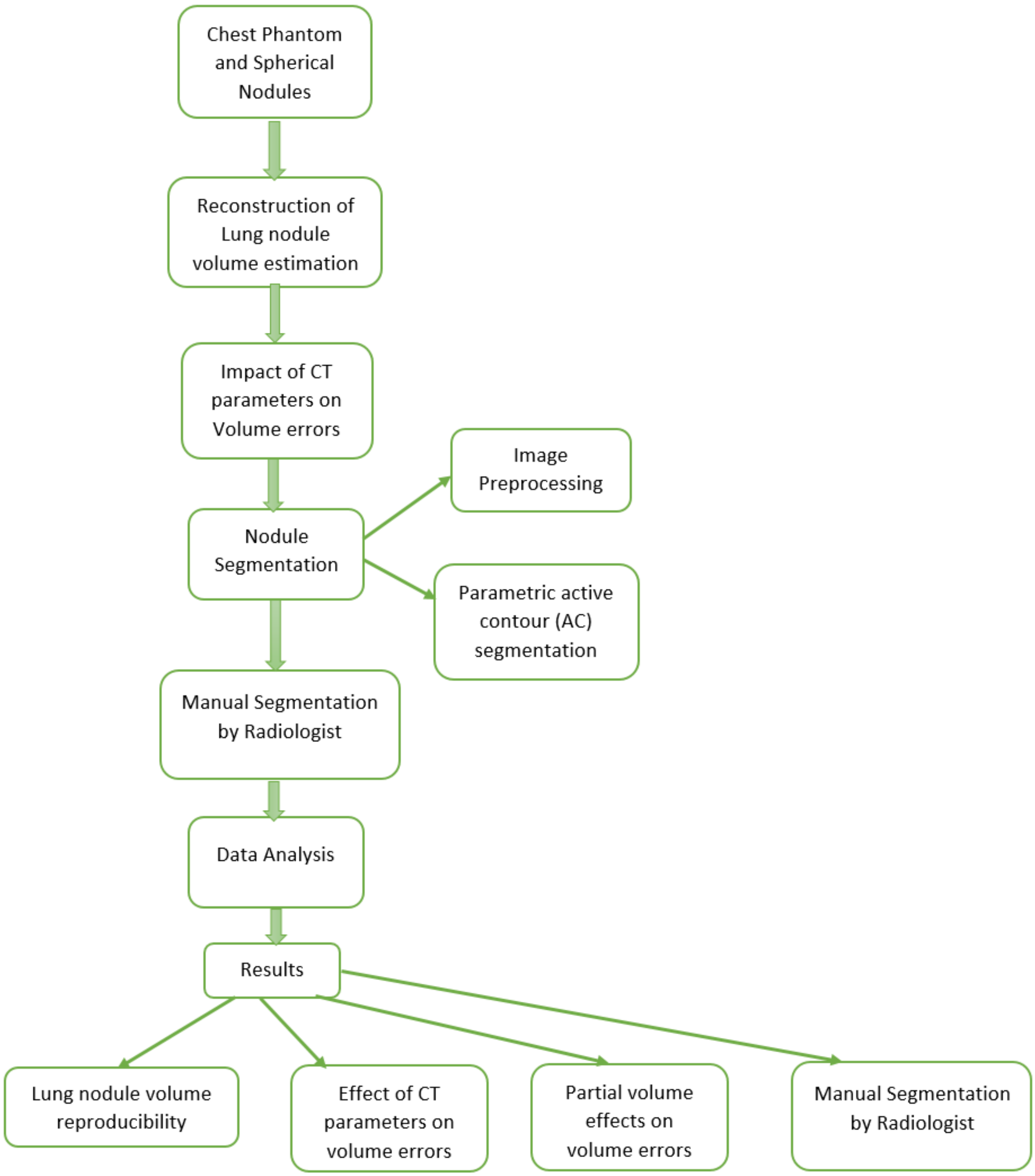

Figure A: Flowchart showing the methodology used.

B. *Chest phantom and spherical nodules*

The chest phantom comprised of a CIRS Model 003 tissue equal transaxial thorax segment phantom (CIRS, Norfolk, VA) sandwiched between two huge water-identical bolus areas. The body shape and lung pits of the water bolus segments coordinate those of the thorax segment. The lung holes in the thorax segment were loaded with a froth that has comparative CT number Hounsfield Units (HU) as lung tissue in CT scans. Nodule mimicking spheres of distances across 4.8 mm, 9.5 mm, and 16 mm were scanned to assess the reliance on knob measure. They were embedded in openings cut in the foam of the lung segment. The interface between areas was loaded with Vaseline to limit air holes.

In Experiment I, five 4.8-diameter 50 mg/cc CaCO3 circles were set in the left lung pit, and six 4.8-mm-diameter 100 mg/cc CaCO3 circles were set in the right lung pit. In Experiment II, scans taken five months after, 10 knobs of a similar size were put in the thorax segment phantom. Five CaCO3 spheres of 50 mg/cc were put in the right lung depression, and five 100 mg/cc circles were set in the left lung hole. After scanning was finished for one size (e.g. 4.8 mm), every one of the 10 circles were supplanted with those of another size (e.g. 9.5 mm).

C. *Reconstruction of lung nodule volume estimation*

CT scans were procured with a GE LightSpeed VCT 64 slice scanner working in 20 mm collimation mode. Pictures were procured in two sessions (Experiment I and Experiment II) five months separated. Inside each examination, three scans (Scans 1, 2, and 3) utilizing indistinguishable parameters were taken for each imaging condition. A similar imaging conditions were utilized as a part of Experiments I and II to reenact serial exams where a subsequent output would be taken months after the fact. In this manner, inconstancy between the two examinations and inside each examination can be evaluated.

We concentrated on conventions utilized with GE 16-slice scanners in two clinical trials. These conditions were utilized in light of the fact that neither one of the trials had distributed conventions for the new 64-slice scanners at the time we started our review, and the 64-slice scanner could be worked in a 20-mm collimation rather than 40-mm collimation mode, which is like that of the 16-slice scanners. The principal wellspring of parameters was the National Lung Screening Trial (NLST), supported by the National Cancer Institute (NCI), which enlisted more than 50,000 high-hazard subjects to look at the viability of CT and chest radiography in lung cancer discovery. Scans on GE 16-slice scanners were procured with the 16 ×1.25 mm indicator arrangement, 120 kVp, 80 mA, 0.5 sec turn time, and 1.375:1 pitch. The second source was the Lung Tissue Resource Consortium (LTRC), supported by the National Heart, Lung and Blood Institute, the objective of which was to make a lung tissue database to comprehend the pathogenetic systems of lung infections. CT scans were gathered as a component of the procedure. Scans on GE 16-slice scanners were procured at 140 kVp, 300 mA, and 0.5 sec revolution time, 1.375:1 pitch. Since both are huge scale studies, and members in the NLST experienced numerous scans over time, exactness and reproducibility under these CT conventions are of intrigue. The imaging conditions for the reproducibility study are recorded in Table A. An extra high determination imaging condition was picked in foresight of thin-slice scans that may turn out to be more typical with multi detector row CT scanners, whose details are given in the table below.

Protocol	Pitch	Slice thickness (mm)	Slice Interval (mm)
Hi-resolution	0.531:1	0.625	0.625
NLST initial	1.375:1	1.25	1.25
NLST retrospective	1.375:1	2.5	2.00
LTRC initial	1.375:1	1.25	0.625
LTRC retrospective	1.375:1	2.5	0.625

Table A: Imaging conditions for the reproducibility study

D. *Impact of CT parameters on volume errors*

For the investigation of the impacts of CT scanning and recreation parameters on nodule volume estimation, every parameter was changed in a range that might be utilized as a part of clinical evaluations. The range is shown in Table B.

Parameter	Changing range
Pitch	0.531:1 to 1.375:1
Slice thickness (mm)	0.625 to 2.5
Tube current (mA)	80 to 400
Field of view (cm)	25 to 36

Table B: Range of variation used for each parameter for the study

E. *Segmentation of Nodule*

Image Pre-processing: A CT scan input to the division program is first preprocessed to get isotropic voxels. Linear interpolation in the z-axis is performed if the recreated slice interim of the CT scan is more noteworthy than the pixel measure on the axial plane. Bilinear interpolation in the axial plane is utilized rather if the slice interim is littler. The interpolation does not enhance the spatial resolution of the CT information, yet it is performed to encourage the usage of the 3-dimensional (3D) division operations. Utilizing a graphical UI, every nodule location is physically distinguished by setting a box that contains the nodule on one scan in light of visual examination. For different outputs where the knobs are in similar positions, a programmed knob identification program extricates volumes of-interest (VOIs) from the scan. The programmed discovery is not a piece of this review but rather is utilized to diminish the time of generally physically marking VOIs. For nodules that are near the pleura, the VOI may incorporate voxels from the pleura and the chest wall. For these nodules, a lung region masking program already created in our research center is connected to the VOI to avoid these voxels from further processing.

Parametric active contour segmentation: Deformable contour models, especially the AC model, are outstanding apparatuses for image segmentation. ACs are energy limiting splines guided by different powers, or energies. We executed a parametric model, representing the contour as vertices of a polygon, and limited it in light of greedy algorithm depicted by Williams and Shah. We executed two new energies to exploit 3D volumetric information and one energy to penalize the aggregate energy if the contour develops into the chest and mediastinum. In this review, we connected the 3DAC model prepared on patient nodules to the division of phantom nodules on CT scans. An underlying form for the nodule in the VOI is created utilizing a k-means clustering and object identification method is utilized to initialize the 3DAC.

F. *Physical Segmentation by Radiologist*

To give a reference to examination with the 3DAC forms, a cooperation trained thoracic radiologist physically sectioned some 4.8-mm-diameter nodules. We chose three scanning conditions, which were indistinguishable with the exception of slice thickness estimations of 0.625, 1.25, and 2.5 mm. The radiologist divided the five 4.8-mm diameter knobs with 100 mg/cc density in the right lung of the chest phantom. There was an aggregate of 15 physically sectioned knobs from the five knobs and three diverse slice thickness conditions.

The radiologist was demonstrated a picture with knobs and was just educated that the phantom knobs were round, without being given any size data. A graphical-UI (GUI) program created in our lab showed a zoomed in ROI containing the knob to be sectioned. The radiologist was allowed to change the brightness and contrast of the image. He was told to plot the knob taking after where he judged to be the nodule boundary in the picture. The shapes were represented by a polygon, and a vertex of the polygon was made where the radiologist clicked on the screen. Since the 3DAC outcome is also a polygon, this permitted coordinate examination of volumes. The radiologist was permitted as much time as he felt agreeable in utilizing the interface and was prepared to utilize the interface utilizing nodules that were not a piece of the physically sectioned data set.

G. ***Data Analysis***

The volume of a fragmented phantom nodule (V3DAC) was figured by multiplying the quantity of voxels contained in the shapes with the volume of each voxel. The divided volume was contrasted and the ground-truth volume of the phantom nodule (Vtrue) and the distinction was accounted for as the rate volume error given in Equation below.

$\%\text{Vol err} = ((V_{3DAC} - V_{true})/\ V_{true}) \times 100\%$ where $V_{true} = (4/3)\pi r^3$

III. RESULTS

A. ***Lung nodule volume reproducibility***

All knob imitating circles were effectively sectioned as judged by visual assessment. A similar imaging conditions were utilized as a part of the two experiments led five months separated. The volume errors were examined independently for every thickness (either 50 or 100 mg/cc of CaCO3) and each scan. Six averages for each imaging condition are recorded for each analysis, since there were three scans taken for every constraint. This was analyzed based on density, reproducibility and volume error variability.

In the analysis by density, the two-tailed paired *t*-test was done where each pair comprised of the mean volume error of 50 mg/cc and 100 mg/cc densities in one scan. The volume blunder difference between the densities was not factually noteworthy ($p = 0.845$). The reproducibility analysis is mainly to decide if there were contrasts in the volume errors among the three indistinguishable scans obtained around the same time, investigation of variance was performed on the three indistinguishable scans. The distinction in the volume estimations ($p > 0.05$) between the scans procured five months separated did not accomplish measurable noteworthiness, for each of the five imaging conditions in Experiments I and II. In the volume error variability analysis, it has been found that, higher variability of volume mistakes happened with bigger slice thicknesses and slice interims. The best volume mistakes happened for the scan utilizing 2.5 mm slice thickness and 2.0 mm slice interim, which were the most minimal resolution scans in this reproducibility study.

B. ***Impact of CT parameters on volume errors***

The impact of CT parameters on volume errors have been studied and the results of the analysis based on the dependence of slice thickness, pitch, field of view and tube currents have been given below in Table C.

CT Parameter	Impact on Volume error
Pitch	No statistically significant effect
Slice thickness (mm)	• Volume error increases as slice thickness increases for a given nodule size. • Volume error decreases as nodule size decreases.
Tube current (mA)	No statistically significant effect
Field of view (cm)	No statistically significant effect

Table C: Impact on volume error caused by CT parameters

Reliance on Slice thickness: The volume error expanded as slice thickness expanded for a given knob estimate and diminished as the knob measure expanded. Changing slice thickness from 0.625 mm to 1.25 mm did not altogether ($p > 0.006$) influence the normal volume mistake. In any case, an adjustment in slice thickness from 1.25 mm to 2.5 mm was factually critical ($p < 0.006$) for the 4.8 mm and 9.5 mm circles, yet did not accomplish measurable hugeness for the 16 mm circles ($p = 0.007$).

Reliance on Tube current: There was no factually noteworthy change (all $p > 0.6$) in normal volume mistakes when slice thickness changed from 0.625 to 1.25 mm for the 100, 200, and 400 mA scans. Notwithstanding, additionally increment in slice thickness from 0.625 mm or 1.25 mm to 2.5 mm brought about a measurably noteworthy ($p < 0.0056$) distinction in mean volume error for all tube currents.

Reliance on Pitch: The difference in pitch did not critically impact the volume error of separation ($p > 0.05$) within the range reviewed for all sizes of nodules.

Reliance on Field-of-View: The mean volume errors of the 4.8, 9.5, and 16 mm circles ranged from 20.3% to 22.4%, 10.3 to 12.4%, and −1.0% to −0.1% correspondingly. There was no statistically critical impact ($p > 0.006$, Bonferroni correction) in the mean volume errors within the range of FOV reviewed.

C. *Partial volume effects on volume errors*

The overestimation in knob volume is basically brought on by partial volume impacts. Normal sectioned contours for the 4.8 mm knob at three slice thicknesses and the same 0.625 mm slice interim are appeared in Figure 6 in the paper. The fragmented limits are outwardly sensible despite the fact that the average volume errors of 20% to 45% appear to be over the top. The segmented volume increments as slice thickness increments in spite of the fact that the genuine nodule size is the same. To additionally exhibit the impact, a circular object of radius 4.8 mm was carefully produced. Examination of both the carefully created slices and the genuine CT slices demonstrated that partial volume impacts for the most part make the volume seem bigger than the genuine volume. This is on the grounds that the knob limit is blurred and more pixels that are outside the genuine knob limit become plainly brighter and are considered some portion of the knob. There are likewise extra slices that seem to contain some portion of the knob while the genuine knob might not have crossed those slices. These impacts end up noticeably more powerful when the slice thickness increments.

D. ***Physical segmentation by a Radiologist***

Figure 8 in the paper demonstrates a correlation of a PC produced edge of a discretized 4.8 mm sphere, the 3DAC outcome, and the radiologist's hand-drawn edges. The mean volume errors of the physically portioned volumes for the five 4.8-mm-measurement knobs in each of the 0.625, 1.25, and 2.5 mm slice thicknesses were 239.3 ± 36.5%, 214.8 ± 34.4%, and 275.6 ± 40.3%, individually. The corresponding 3DAC mean volume errors for similar knobs and imaging conditions were 18.6 ± 5.5%, 23.6 ± 7.6%, and 45.2 ± 5.4%, separately.

IV. OVERALL REVIEW AND DISCUSSION

In this paper, our concentration is to assess the impacts of CT scanning and recreation parameters on the precision and reproducibility of mechanized knob volume estimation. Despite the fact that the outright extent of the volume errors evaluated utilizing phantom nodules might be not quite the same as those of genuine nodules in patient scans, this review uncovers imperative patterns for the reliance of the volume errors on CT imaging conditions and the fluctuation of these estimations. This data may fill in as a guide when robotized or manual techniques are utilized to evaluate interim volume change of a knob from serial CT scans.

Our review demonstrated that the average volume error in respect to the ground truth were reliably overestimated, aside from the 16 mm knobs at thin slice thickness that every so often indicated slight underestimation inside exploratory instabilities. The overestimation is basically brought about by fractional volume averaging instead of the computerized AC segmentation settings as exhibited in our examination of the partial volume impact. Knob size and slice thickness had the biggest consequences for the deliberate volume precision. For a given CT condition, the littler the knobs, the higher the rate volume errors.

In this review, regular CT scans have 0.703 mm determination in the pivotal plane. The voxels are isotropic after insertion to a volume of (0.703)3 mm3. At this voxel estimate, a 4.8 mm distance across circle contains roughly 168 voxels if the impact of discretization is overlooked. Seven slices (4.8 mm/0.703 mm) is the most modest number of slices that can represent this nodule. A 20% over-estimation in volume is the consequence of 33 additional voxels, which compares to under five pixels for every slice. As such, if five more voxels in each slice are considered some portion of the knob rather than the background for each slice, it will bring about a 20% volume error. In this manner, the volume error for little knobs is particularly touchy to the vulnerabilities in the fragmented boundary, as a slight deviation because of partial volume impact and recreation artefacts, for example, a blurry or unpredictable edge would bring about generous percentage error. At the point when the slice thickness is substantial, the blurry limit because of partial volume averaging adds to additional slices for the knob. The extra slices and extra voxels in each slice together would have brought about the high-volume errors (>40% for 2.5 mm slice thicknesses) for the 4.8 mm knobs.

This is differentiated to a review by Yankelevitz et al. that revealed volume errors of ±3% for 3.2 and 3.96 mm measurement phantom nodules (Yankelevitz et al., 2000). The distinction might be credited to two fundamental components. To begin with, Yankelevitz et al. scanned the phantom at a high resolution of 1 mm bar collimation and 9.6 cm FOV, bringing about pixel size of 0.188 × 0.188 mm in the axial plane, with remade slice interim of 0.5 mm and trilinear interpolation to get isotropic voxels. In our review, the littlest slice interim of 0.625 mm would have brought about interpolated isotropic voxels with volumes of 0.244 mm3, which is 36.7 times bigger than their isotropic voxels with volumes of 0.00665 mm3 (=0.1883). Second, our AC parameters were trained with patient knobs as opposed to the present set of phantom nodules. We can expect that if the AC parameters were prepared to fit the edge attributes of phantom nodules, the AC portioned volumes could be changed in accordance with be nearer to their ground-truth volumes. Nonetheless, the subsequent AC calculation may not perform well for patient knobs. Since division of patient knobs is the objective for building up the mechanized AC technique, we applied the trained AC to phantom nodules without re-preparing.

There was likewise no measurably critical impact of FOV on the average volume error, in spite of the fact that the average volume error for the 36 cm FOV was reliably somewhat lower than that for the 25 cm or 30 cm FOV. There was no measurably noteworthy reliance of volume mistakes on tube current for pitch settings of 0.531:1 and 1.375:1 and for slice thicknesses from 0.625 mm to 2.5 mm. The volume errors in this way were moderately autonomous of measurements for the phantom nodules. For appraisal of knob development, it might be adequate to utilize high resolution however low dosage serial scans.

We have exhibited that there is a huge contrast in the assessed volume when the CT scan is gained with various imaging conditions. To limit the error, thin slice CT scans ought to be utilized, particularly for little knobs. Moreover, to assess the development of a knob, it is critical to utilize a similar scanning and remaking parameters in follow-up scans. At present, follow-up scanning is performed for knobs after certain time interims, yet there are no particulars on the parameters to be utilized. A benchmark scan and follow-up scan utilizing diverse slice thicknesses, for instance, may bring about comparative volume estimations when in reality the knob measure has changed. The error in volume change estimation may prompt misdiagnosis and postponement in treatment. The volume errors additionally bring up issues with respect to conventions used to screen for lung tumor.

In clinical CT scans, inconstancies, for example, patient movement and the adjustment in knob size and boundary attributes after some time will additionally debase the reproducibility between serial exams. Besides, clinical knobs are not so much sharp but rather more unpredictable limits than round phantom nodules. These qualities may bring about extra volume errors contrasted and those evaluated in this review, and cause vast inter and intra observer inconstancies notwithstanding for experienced chest radiologists.

V. Limiting Conditions

There are constraints in this review. To start with, we incorporated a moderately extensive variety of knob sizes to give general patterns, yet it is valuable to research more sizes in the 3 mm to 9 mm diameter range, since knobs of these sizes are regularly followed-up on CT. Second, it will be of solid enthusiasm to gauge the littlest conceivable volume change that can be evaluated with certainty utilizing computerized division. Third, it is not known whether similar patterns seen in this phantom study would be seen for true lung knobs. Fourth, it is likewise not known whether the reliance of volume errors on imaging and recreation parameters is predictable for CT scans obtained with scanners from various makers. Fifth, for the assessment of CT parameters on volume errors, we settled the slice interim at 0.625 mm to lessen the quantity of factors. The impacts of this parameter and its collaboration with different parameters on volume mistake are still obscure. At last, we didn't implement targeted recreations with littler FOVs, for example, 9.6 cm that would decrease volume averaging in the axial plane. These and other different issues will be examined in future reviews.

VI. COMPARATIVE STUDY WITH OTHER METHODS

The main aim of *Petrou et al* was to survey contrasts in volumetric estimations of aspiratory knobs got utilizing distinctive CT slice thicknesses; relate these distinctions with knob size, shape, and margination; and look at estimations created by two diverse software packages. Seventy-five individual knobs recognized on 29 lowdose, unenhanced, MDCT chest examinations were chosen for volumetric investigation. Every image data was recreated in three ways. Volume changeability between various slice thicknesses was connected with knob breadth, shape, and margination utilizing numerous linear regression. Percent contrasts between estimations gotten with the two programming frameworks were ascertained. Centrality of relative volume contrasts between slice thicknesses and software packages was surveyed utilizing a one-example Student's t-test. CT slice thickness variety brought about noteworthy contrasts in volume estimations for minor knobs. A spiculated edge was appeared to significantly affect knob volume inconstancy inside a solitary size group. Utilization of various programming frameworks brought about noteworthy volume estimation contrasts at the 2.5-mm CT slice thickness.

The major motivation of *Ravenel et al* was to tentatively assess in a phantom the impacts of recreation portion, field of view (FOV), and area thickness on computerized estimations of aspiratory knob volume. Round and lobulated pulmonary knobs 3–15 mm in breadth were set in a generally accessible lung phantom and filtered by utilizing a 16-section CT scanner. Tests were performed to assess seven recreation filters and the autonomous impacts of FOV and area thickness. Mechanized knob volume estimations were performed by utilizing PC helped volume estimation programming framework. General linear regression models were utilized to look at the autonomous impacts of every parameter, with rate overestimation of volume as the needy variable of intrigue. Results show that there was no generous contrast in the precision of volume estimations over the seven remaking kernels. There was significant overestimation of the volumes of the 3–5-mm knobs measured by utilizing the volume estimation programming framework. Diminishing the FOV encouraged no huge change in the exactness of lobulated knob volume estimations. The exactness of volume estimations—especially those for little knobs—was altogether ($P < .0001$) influenced by segment thickness.

VII. CONCLUSION

Methods/Data based conclusion: In conclusion, we have found that scanning and reproduction parameters of CT scans influence programmed volume estimation by the 3DAC technique. This examination has critical clinical ramifications since contrasting knob volumes measured from two distinct scans to decide if there is development is a usually utilized technique in introductory diagnosis of lung tumors. In the bigger setting of an computerized image analysis system, this demonstrates not only the division algorithm is vital, the technique for picture procurement for the CT scans utilized as a part of the division likewise influences the result. Consequently, to precisely catch up on a nodule to distinguish interim change in volume, the scanning and recreation parameters ought to be appropriately picked and kept consistent between the initial and follow-up scans to limit the changeability in the volume change assessment.

Future works/Direction: The CT scanning pitch did not fundamentally influence volume error ($p > 0.05$) for phantom nodules of all sizes when alternate parameters were settled as picked in this review. Be that as it may, this investigation was performed for thin slices (0.625 mm thickness and interim). Future analyses are expected to decide if this outcome would at present hold with bigger slice thicknesses and interims.

VIII. REFERENCES

[1] Ted W. Way, Heang-Ping Chan, Berkman Sahiner, Mitchell M. Goodsitt, Lubomir M. Hadjiiski, Chuan Zhou, and Aamer Chughtai " Effect of CT scanning parameters on volumetric measurements of pulmonary nodules by 3D active contour segmentation: A phantom study". Radilogy.

[2] Harris K, Adams H, Lloyd D, Harvey D. The effect on apparent size of simulated pulmonary nodules of using three standard CT window settings. Clin Radiol 1993;47:241–244. [PubMed: 8495570]

[3] Winer-Muram HT, Jennings SG, Meyer CA, Liang Y, Aisen AM, Tarver RD, McGarry RC. Effect of varying CT section width on volumetric measurement of lung tumors and application of compensatory equations. Radiology 2003;229:184–194. [PubMed: 14519875]

[4] Meyer CR, Johnson TD, McLennan G, Aberle DR, Kazerooni EA, MacMahon H, Mullan BF, Yankelevitz DF, van Beek EJR, Armato SG III. Evaluation of lung MDCT nodule annotation across radiologists and methods. Academic Radiology 2006;13:1254–1265. [PubMed: 16979075]

[5] Yankelevitz D, Reeves A, Kostis W, Zhao B, Henschke C. Small pulmonary nodules: volumetrically determined growth rates based on CT evaluation. Radiology 2000;217:251–256. [PubMed: 11012453]

[6] Yankelevitz DF, Gupta R, Zhao B, Henschke CI. Small pulmonary nodules: evaluation with repeat CT - Preliminary experience. Radiology 1999;212:561–566. [PubMed: 10429718]

[7] Zerhouni EA, Spivey JF, Morgan RH, Leo FP, Stitik FP, Siegelman SS. Factors influencing quantitative CT measurements of solitary pulmonary nodules. JCAT 1982;6:1075–1087.

[8] Ko JP, Rusinek H, Jacobs EL, Babb JS, Betke M, McGuinness G, Naidich DP. Small pulmonary nodules: volume measurement at chest CT—phantom study. Radiology 2003;223:864–870. [PubMed: 12954901]

[9] Goo JM, Tongdee T, Tongdee R, Yeo K, Hildebolt CF, Bae KT. Volumetric measurement of synthetic lung nodules with multi-detector row CT: effect of various image reconstruction parameters and segmentation thresholds on measurement accuracy. Radiology 2005;235:850–856. [PubMed: 15914478]

[10] James G. Ravenel, MD, William M. Leue, BA, Paul J Nietert, PhD, James V. Miller, PhD, Katherine K. Taylor, MS, and Gerard A. Silvestri, MD, MS "Effect of Reconstruction Parameters on Automated Volume Measurements of Pulmonary Nodules: A Phantom Study". Radiology

[11] Myria Petrou, Leslie E. Quint, Bin Nan, Laurence H. Baker "Pulmonary Nodule Volumetric Measurement Variability as a Function of CT Slice Thickness and Nodule Morphology". Chest Imaging – Original Research.